

Structure of SST and Surface Wind Variability during Indian Ocean Dipole Mode Events: COADS Observations*

N. H. SAJI⁺

Institute for Global Change Research, Kanagawa, Japan

T. YAMAGATA

Institute for Global Change Research, Kanagawa, and The University of Tokyo, Tokyo, Japan

(Manuscript received 19 July 2002, in final form 16 December 2002)

ABSTRACT

A study of the detailed spatiotemporal characteristics of the Indian Ocean dipole (IOD) mode in SST and surface winds using available observations from 1958 till 1997 is reported. The analysis is used to address several of the controversial issues regarding the IOD.

One key finding of this study is that interdecadal fluctuations contribute strongly to tropical Indian Ocean (TIO) SST variability; in SST anomalies (SSTA) interdecadal variance is as strong as interannual variance. Over both the western and eastern TIO, an accelerated warming of SST after the mid-1970s is apparent. The lack of anticorrelation between western and eastern TIO SSTA occurs only in this latter half of the analysis period.

In order to examine the hypothesis that the IOD is a part of ENSO evolution in the TIO, the temporal characteristics of IOD indices have been compared with Niño-3. On the basis of several quantitative comparisons that include wavelet and cross-wavelet analysis, several important differences between the two phenomena are reported. These differences are highlighted to argue that the IOD is not a part of ENSO evolution in the TIO. On the other hand, a striking similarity is found in the temporal structure of atmospheric and oceanic variability within the TIO that is suggestive of IOD arising from inherent coupled air-sea interactions in the TIO.

ENSO events that do not co-occur with IOD have been isolated and their impacts on TIO SSTA and winds described. Similarly, the characteristics of IOD events that occur independently of ENSO are described. Based on the characteristics of these two groups a hypothesis is suggested through which both phenomena may interact. It is noted that ENSO events co-occurring with IOD events are much stronger compared to non-co-occurring events. On the other hand, IOD events that are independent of ENSO as well as those that co-occur with it appear to have the same strength.

1. Introduction

An interannual climate anomaly characterized by a sea surface temperature (SST) anomaly (SSTA) of opposing sign in the western and eastern tropical Indian Ocean (TIO) has been recently reported (Saji et al. 1999, hereafter S99). Strong zonal wind anomalies trapped to the equatorial Indian Ocean are a characteristic atmospheric feature during such SSTA events (Reverdin et al. 1986; S99; Webster et al. 1999; Murtugudde et al. 2000). From satellite-derived and in situ observations it is also seen that these events are associated with sea level (Rao et al. 2002; Feng et al. 2001; Feng and Mey-

ers 2003) and rain anomalies (S99; Saji and Yamagata 2003, manuscript submitted to *Climate Res.*, hereafter SY) having a similar structure as the SSTA. In this paper, we refer to this climate anomaly as the Indian Ocean dipole (IOD) mode event. For a short review of the phenomenon in relation to the monsoon circulation of the TIO, see Schott and McCreary (2001).

The dipolelike SSTA characterizing the IOD was mentioned in a few research articles on TIO variability (Reverdin et al. 1986; Flohn 1987; Nicholls 1989; Hastenrath et al. 1993; Meyers 1996) since the 1980s. However, these anomalous conditions in the TIO have gained wider notice since the recent occurrence of two strong events: that of 1994 (Meyers 1996; Behera et al. 1999; Reppin et al. 1999; Vinayachandran et al. 1999) and that of 1997 (Chambers et al. 1999; Webster et al. 1999; Yu and Rienecker 1999; Murtugudde et al. 2000).

Several recent studies discussed the oceanic processes involved during IOD events (Murtugudde et al. 2000; Feng et al. 2001; Rao et al. 2002; Li et al. 2002; Feng and Meyers 2003). Others explored its impact on local

* International Pacific Research Center Contribution Number 197.

⁺ Current affiliation: International Pacific Research Center, University of Hawaii at Manoa, Honolulu, Hawaii.

Corresponding author address: Dr. N. H. Saji, IPRC, 2525 Correa Rd., University of Hawaii at Manoa, Honolulu, HI 96822.
E-mail: saji@hawaii.edu

and global climate (Ashok et al. 2001; Clark et al. 2003; Behera and Yamagata 2003; SY). However, as discussed below, the results of some new studies have generated a somewhat fierce controversy on various aspects of this phenomenon. An objective of this study is to address these controversial questions on the basis of data analysis. We approach these controversies through a detailed examination of the spatiotemporal structure of IOD variability in TIO SST and winds and their relation to El Niño-Southern Oscillation (ENSO) variability. Consequently, an important outcome of this study is a detailed description of the spatiotemporal character of the IOD phenomenon.

One controversial topic is the relation of SST variability in the eastern and western TIO during IOD events. The composite analysis of S99 implied an out-of-phase SSTA relation between the eastern and western TIO. However, correlation analysis shows that the western and eastern TIO SSTAs are not significantly anticorrelated (Dommengat and Latif 2002; Nicholls and Drosowsky 2001). This suggests that the SSTA pattern associated with IOD may be a zonal gradient perturbation on a uniformly signed basinwide anomaly (Hastenrath 2002).

Another issue of much debate is the relation of IOD events to ENSO. Some studies claimed IOD to be an inherent coupled mode of the TIO, independent of ENSO. S99 noted that many positive IOD events occurred either in the absence of El Niño or sometimes even with a La Niña. Further, they pointed out that the monthly time series of the zonal SST gradient, also referred to as dipole mode index (DMI), is only moderately correlated with the Niño-3 (5°N – 5°S , 90° – 150°W) index but that of DMI and equatorial winds over the Indian Ocean (U_{eq}) are more strongly correlated. Webster et al. (1999) synthesized observations of sea level, wind, SST, and outgoing longwave radiation (OLR) anomalies to demonstrate the role of wind-forced ocean dynamics in creating the IOD SSTA pattern and, conversely, the effect of the SSTA on OLR and wind fields.

Nevertheless, seasonally stratified correlation for the boreal fall season between the IOD and ENSO indices is highly significant (Nicholls and Drosowsky 2001; Baquero-Bernal and Latif 2002; Hendon 2003). In an earlier study, Hastenrath et al. (1993) noted a statistical association, during boreal fall, between ENSO indices and SSTA of opposing sign in the eastern and western TIO.

The rest of the paper is organized as follows. In section 2 we describe the data and the reason for using the Comprehensive Ocean–Atmosphere Data Set (COADS) observations for this analysis. Composite analysis is used in section 3 to briefly introduce the relevant features of the IOD event. In section 4 we present a correlation analysis of SSTA between the western and eastern TIO. Raw SSTA is analyzed first and then repeated after linear trends, interdecadal anomalies, and ENSO-

lagged effects are successively filtered out. A multivariate definition of IOD is proposed in section 5. On the basis of this definition 19 IOD events of both phases are identified and composited to define a canonical IOD event. The contribution of these 19 events to TIO interannual variability is assessed in section 6. In section 7 we compare time series of DMI and Niño-3 and, in section 8, those of DMI and U_{eq} . Based on the results from sections 3–8, we discuss the various controversial issues associated with IOD in section 9. Important results are summarized in the last section.

2. Data

Presatellite era SST data, being based on conventional measurements along ship tracks, are temporally and spatially inhomogeneous. There are several homogeneously gridded SST products that use different methods to fill in the data between ship tracks. A very popular method (e.g., Kaplan et al. 1998; Rayner et al. 1996) bases the interpolation/extrapolation process on structures derived from EOF analysis of satellite era SSTA. However, since the EOFs can be artificial structures (von Storch and Zwiers 1999), one may doubt the reality of the “virtual” SST values in the data gaps. Further, there are issues about the statistical stationarity of the structures captured in such EOF modes. On the other hand, more conventional interpolation methods inevitably introduce assumptions about the spatial and temporal distribution of the SST.

In view of the above considerations we have used only real SST and wind data along ship tracks for this study. Quality-controlled data from the COADS project (Woodruff et al. 1998) available in evenly spaced $2^{\circ} \times 2^{\circ}$ bins at monthly resolution are used. In the enhanced version of the COADS release 1c data, that we have used here, the data are trimmed using climatological 4.5 standard deviation limits to better represent extreme climate events. Though these reports are based mostly on quality-controlled marine surface observations from ships, they have been supplemented in more recent years to include moored environmental buoys, drifting buoys, and near-surface measurements from oceanographic profiles.

The analysis period for this study is 40 years from January 1958 to December 1997. Reasonably good spatial and temporal data coverage in the regions of interest for our study exists during this period. Anomalies were computed by subtracting the climatological seasonal cycle from the data. Except where mentioned, the analyses are performed on unfiltered data.

3. Composite analysis of cold events in the eastern TIO

Figure 1 depicts the interannual anomaly of the boreal fall season [September–October–November, (SON)] SSTA (thick line) from a single $2^{\circ} \times 2^{\circ}$ box (E1) cen-

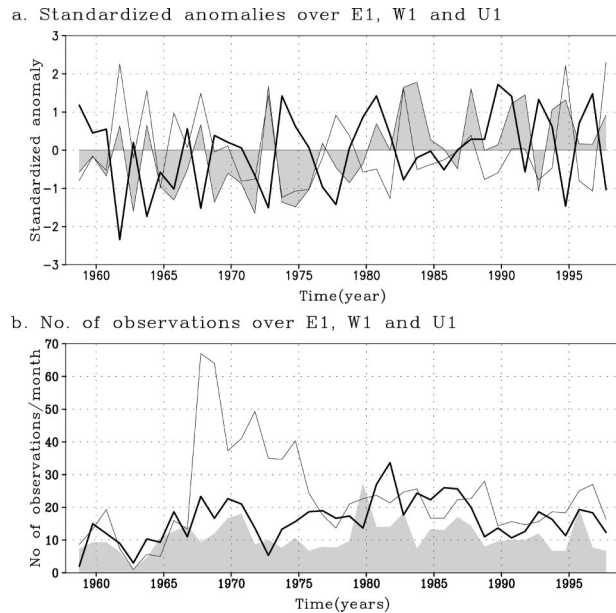


FIG. 1. (a) SST anomalies at E1 (7°S , 105°E) and at W1 (3°S , 71°E) are represented by the solid thick line and the gray-filled line, respectively. The solid thin line is the sign-reversed zonal wind anomaly at U1 (1°S , 85°E). All anomalies were standardized using their respective std dev ($\sigma_{E1} = 0.5$, $\sigma_{W1} = 0.4$, $\sigma_{U1} = 2.6$). (b) Same as in (a), but for the average number of observations per month at E1, W1, and U1.

tered around 7°S , 105°E . In the period under consideration this box is well sampled (see Fig. 1b), having about 15 observations per month on the average. Thus, the estimate of monthly SST over E1 is fairly reliable. The gray-filled thin curve is the SSTA from a western TIO box (W1; 3°S , 71°E). The thin solid curve depicts the interannual SON anomalies of equatorial zonal wind from U1 (1°S , 85°E). In Fig. 1, the sign of U1 is reversed for clarity. Note that all of the three boxes shown here are well sampled on the average (Fig. 1b). However, the year 1962 is an exception, only about 1–3 observations are available during this year to construct the estimates.

Whereas E1 is positively correlated with U1 (at the 99% level; $r = 0.8$), W1 is negatively correlated with U1 (also at the 99% level; $r = -0.5$). However, E1 and W1 are negatively correlated with each other only at the 95% level ($r = -0.3$). A direct implication of these correlations is that SSTA over E1 and W1 are most likely out of phase whenever there is a strong zonal wind anomaly over U1. On the other hand, the weaker magnitude of the anticorrelation between E1 and W1 relative to that of E1 and U1 (or W1 and U1) suggests that E1 and W1 do not always exhibit the out-of-phase behavior, especially during times of weak zonal wind anomaly. These features of the relation among U1, E1, and W1 can be readily observed in Fig. 1.

Figure 2 shows composite SSTA during SON for seven of the coolest SST years (1961, 1963, 1967, 1972, 1977, 1994, 1997) over E1. The broad picture that

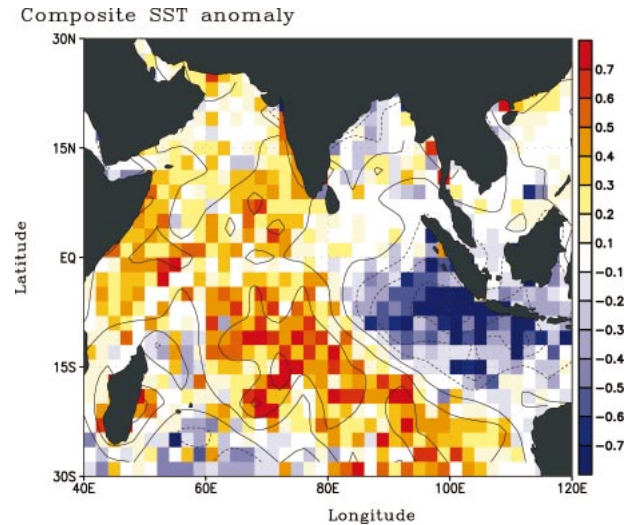


FIG. 2. Composite map of SON SST anomaly based on seven of the coolest SST anomaly years at E1. Contours are at $\pm 0.2^{\circ}$, $\pm 0.4^{\circ}$, $\pm 0.6^{\circ}$, . . . , etc.

emerges is a dipolelike SSTA pattern with large-scale cooling in the eastern TIO but large-scale warming in the western TIO. The cooling is strongest south of the equator trapped to the Indian Ocean coast of Indonesia. A slight cooling is also observed in the Bay of Bengal SST. The warm SSTA is apparent on both sides of the equator. An elongated warm SSTA is seen to stretch in a southwesterly direction toward Australia from the western TIO (cf. Fig. 2 of S99).

The phase lag in the evolution of the SSTA pattern (S99) is important in designing methods to detect the dipolelike structure. To clarify the phase-lagged evolution, we perform below a composite analysis similar to S99, however with the following differences. First, the data are different and are not subjected to filtering. Second, we discuss the composite total SST evolution instead of the anomaly evolution. And third, the composite is indexed by cold SSTA events over E1 mentioned above, as opposed to the zonal SST gradient index used by S99.

For this analysis the data in $2^{\circ} \times 2^{\circ}$ bins are inappropriate since the data points are not homogeneous in space and time. However, the variability associated with IOD is large scale (cf. Fig. 2). Therefore, for the monthly composites presented in Fig. 3, we used SST binned in $10^{\circ} \times 10^{\circ}$ boxes. The resulting area-averaged bins had very few missing points in the regions being examined in this study. These (not more than 5 months in 40 yr, about 1% of the data) were filled in by linear time interpolation.

The results presented in Fig. 3 appear to be consistent with those of S99. Thus, the anomalous SST departure during these events is phase locked to the seasonal cycle. For instance, anomalous warming in the west develops during the season when the climatological SST itself is rising. Similarly the cold SSTA in the eastern boxes

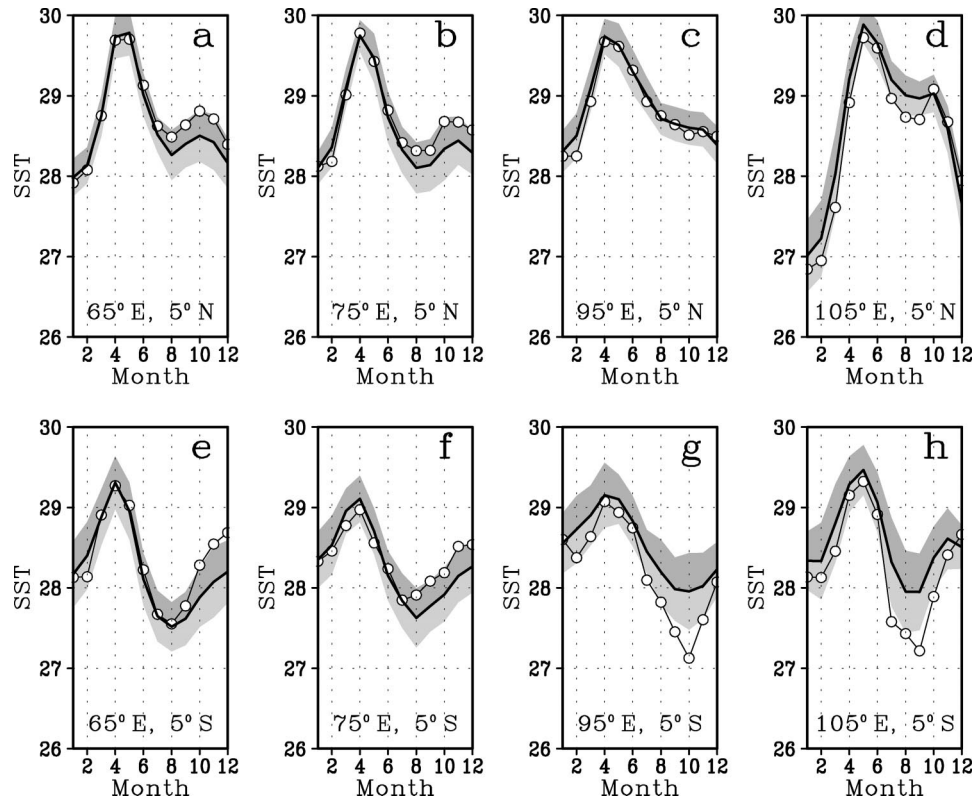


FIG. 3. Composite time series of total SST evolution for the IOD events at locations centered around 5°N and (a) 65° , (b) 75° , (c) 95° , (d) 105°E . (e)–(h) Same as in (a)–(d), except that they are centered around 5°S . The thick black solid line depicts the evolution of the climatological SST at each location. The gray shades on both sides of the climatological time series depict the 1σ envelope of interannual std dev.

develops during the progression of the annual cycle from warm to cool SST. In the eastern boxes south of the equator this has led to an enhanced annual cycle. In contrast, SST from the northeastern boxes exhibits little anomalous behavior.

A phase lag in the SSTA evolution between western and eastern TIO is evident. Cold SSTA develops as early as June/July in the eastern TIO and continues to increase in amplitude until September/October. However, SST in the western TIO begins to depart from climatology only around August/September; thereafter, it continues to be anomalous until the end of the year.

We note that although the IOD signal on TIO SSTA may qualitatively be described as dipolelike, the contribution of the eastern and the western “pole” of the SSTA pattern to total SSTA variability is somewhat different. To show this we have also plotted in Fig. 3 the envelope of raw interannual standard deviation (hereafter σ) for each month. A one standard deviation on either side of the seasonal cycle is indicated by the gray shaded envelope. The composite SST departure in the western TIO is of the same level as the background variability. This indicates that the SST signal in the western TIO is composed of not only the signal associated with the dipole SSTA pattern, but also of other

patterns of variability. Therefore, although the IOD is a significant contributor of SST variability to this region (S99), it is not likely the dominant contributor. In the eastern TIO, on the other hand, the IOD appears to be the dominant contributor to SST variability during the boreal summer [June–July–August (JJA)] and fall seasons.

A stronger signature of the IOD event is apparent in the zonal SSTA gradient and equatorial wind fields. The composite analysis for the zonal SST gradient is shown in Fig. 4e. The zonal SST gradient was estimated as follows. Since the four western Indian Ocean (WIN) boxes had a similar evolution of SST anomaly during IOD years, we binned them into a single western box (WIN; 10°S – 10°N , 60° – 80°E). An eastern box (EIN; 10°S – 0° , 90° – 110°E) was constructed from two of the southeastern Indian Ocean boxes. The zonal SST gradient anomaly is defined as the difference between WIN and EIN. We will refer to this index as DMI following S99. However, our definition of DMI differs slightly from that of S99 in that we center the western box around 70°E in accordance with the information in Fig. 3.

It is noted that the composite zonal SST gradient departure is above the 1σ level during both boreal summer and fall seasons. The same is true for the surface

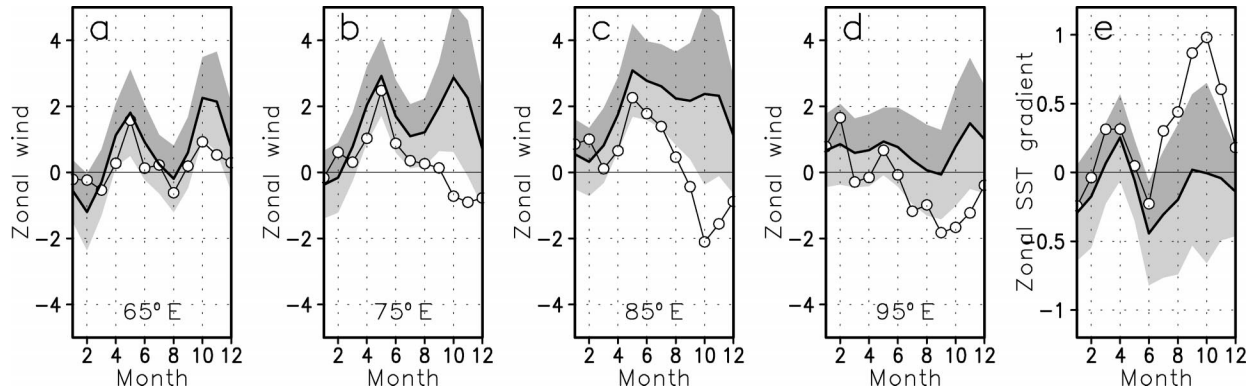


FIG. 4. Same as Fig. 3, except that (a)–(d) are zonal wind anomaly from $2^\circ \times 2^\circ$ boxes centered around 65° , 75° , 85° , and 95° E, respectively, and the equator. (e) The time series is for the zonal SST gradient. The zonal SST gradient is estimated as the difference of SST anomaly between a western box (10°S – 10°N , 60° – 80°E) and an eastern box (10°S – 0° , 90° – 110°E).

zonal wind variability in the central Indian Ocean (IO) as well (Figs. 4c,d). From Fig. 3, it may be surmised that the contribution to the gradient is dominated by eastern TIO SSTA in the boreal summer, while in the boreal fall both the western and eastern TIO SSTAs contribute to it.

4. Correlation between WIN and EIN SSTA

The composite analysis presented above suggests that SSTA between WIN and EIN should be anticorrelated in SON. However, we found that the correlation between

WIN and EIN, using unfiltered data for SON, is statistically insignificant (Table 1). Nevertheless, as in the case of the well-sampled points E1 and W1, there is a strong correlation (see Table 1) of both EIN and WIN with zonal wind anomaly over the equator (U_{eq}), implying that SSTA varies out of phase during strong equatorial wind anomalies (U_{eq} is the area-averaged wind anomaly over 5°S – 5°N , 70° – 90°E).

Together both correlations suggest that patterns of SSTA behavior other than the IOD associated out-of-phase behavior are present in TIO SSTA. Further, it may be hypothesized that it is the presence of such patterns in significant proportions that confound the expression of the IOD SSTA pattern in correlation analysis (Behera et al. 2003). In the following we discuss three possible candidates that may be confounding the expression of anticorrelation between EIN and WIN.

TABLE 1. Cross-correlation matrix for WIN, EIN, DMI, U_{eq} , and Niño-3: (a) for unfiltered data, (b) after filtering linear trend, (c) after also filtering interdecadal anomaly, and (d) after also removing BWA. Correlations significant at the 95% level are italic. Correlations significant at the 99% level are bold.

	Category				
	WIN	EIN	DMI	U_{eq}	Niño-3
a. Unfiltered data					
WIN		-0.06	0.68	-0.54	0.58
EIN			-0.77	0.67	-0.11
DMI				-0.85	0.45
U_{eq}					-0.55
b. After filtering linear trend					
WIN		-0.26	0.75	-0.64	0.49
EIN			-0.83	0.71	-0.3
DMI				-0.85	0.48
U_{eq}					-0.64
c. After also filtering interdecadal anomaly					
WIN		-0.41	0.75	-0.69	0.54
EIN			-0.79	0.81	-0.35
DMI				-0.81	0.47
U_{eq}					-0.65
d. After also filtering BWA					
WIN		-0.52	0.75	-0.69	0.54
EIN			-0.91	0.85	-0.47
DMI				-0.82	0.40
U_{eq}					-0.65

a. Linear trend

Figure 5a shows the result of applying two passes of a 7-yr running mean filter on WIN, EIN, and U_{eq} . Apparently, SST in the Indian Ocean has warmed up by 0.4° – 0.5°C during the course of the 40 years of the study period. On the contrary, no substantial linear trend is apparent in the surface zonal wind field. After filtering out the linear trend from the data, the correlation between WIN and EIN (during SON, $r = -0.26$) became negative and significant only at the 90% level (see Table 1).

b. Interdecadal anomalies

Apparently, the secular trend cannot completely explain the nonstationarity of the means in the data. The 7-yr running mean applied on detrended data (Fig. 5b) captures noticeable low-frequency vacillations of the mean in the TIO surface winds and SST.

The equatorial westerly wind appears to be weaker

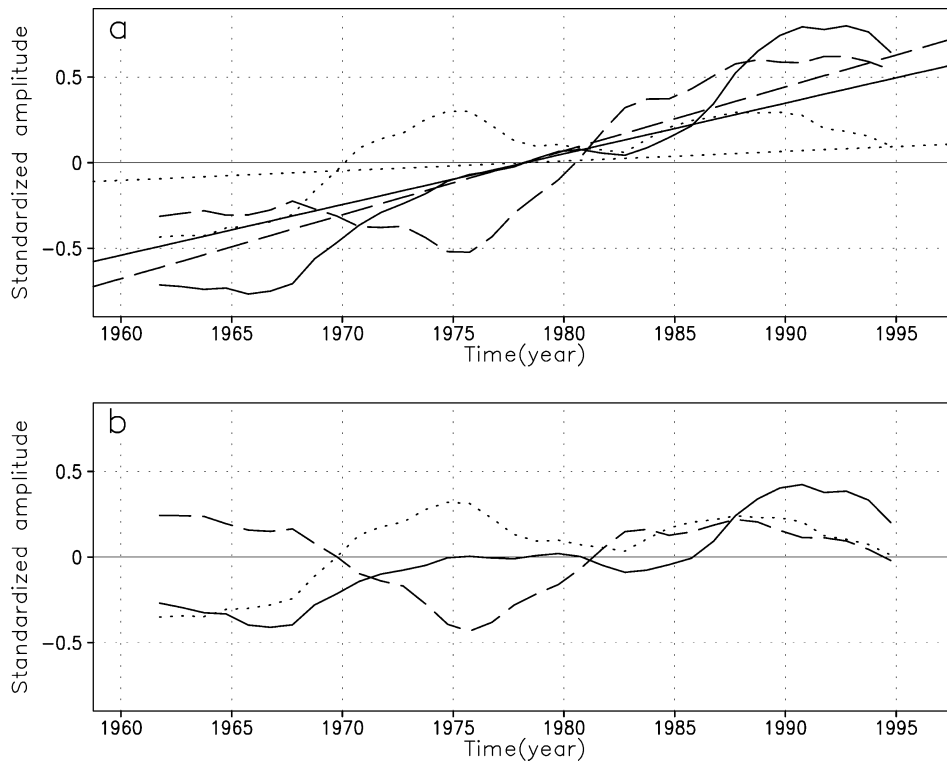


FIG. 5. (a) The time series of SST anomaly over EIN (solid line), WIN (dashed line), and that of zonal wind anomaly over U_{eq} (dotted line) after smoothing using two passes of a 7-yr running mean. The linear trend in the time series is also indicated using the same plotting scheme. (b) Same as in (a) but after detrending the data. To facilitate plotting, all anomalies were standardized using their respective std dev ($\sigma_{EIN} = 0.4$, $\sigma_{WIN} = 0.3$, $\sigma_{U_{eq}} = 1.9$).

than normal during the 1960s and stronger than normal in the 1970s and 1980s. It is noteworthy that these equatorial wind field changes are consistent with the changes of eastern TIO sea level on interdecadal timescales (Clarke and Lebedev 1997).

Figure 5b also implies an unusually warmer mean SST at WIN in the 1960s and from the 1980s onward, and an unusually cooler mean state in between. At EIN, mean SST appears to be cooler before the end of the 1970s relative to the period after that. In both cases an accelerated warming relative to the linear trend appears to have taken place after the late 1970s, around the time of the so-called regime shift (Nitta and Yamada 1989; Royer 1989; Trenberth 1990).

We estimated these interdecadal fluctuations (periodicities longer than 7 yr) applying Fourier analysis on detrended data and filtered them out. It is found that the correlation between WIN and EIN is now highly significant (at the 99% level, $r = -0.41$).

Through Fig. 5, we have portrayed the nature of the trend and the interdecadal fluctuations only for SON. However, it appears that both the secular trend and the interdecadal fluctuations are significantly different from season to season (see Table 2).

c. The lagged ENSO effect on TIO SSTA

It is well known that ENSO has a remote influence on the TIO. One of the manifestations of the ENSO teleconnection is a basinwide warming (cooling) of TIO SST lagging one to two seasons behind an El Niño (La Niña) (Cadet 1985; Wallace et al. 1998; Klein et al. 1999). This ENSO lagged effect illustrated in Fig. 6, by averaging TIO SSTA between 20°S – 20°N and 40° – 100°E , will be referred to as the basinwide anomaly (BWA).

Within the TIO, there is a phase lag in the establishment of the peak anomaly associated with the BWA, with the western TIO leading the eastern TIO by several months to a season (Enfield and Mestas-Nunez 2000). To account for this phase lag in the establishment of the peak anomaly, we regressed monthly WIN and EIN separately on the monthly Niño-3 index at different lags. All the three time series were subjected to a 3-month running mean filter before performing this calculation. The regression coefficient at the lag with maximum correlation was used to estimate the BWA. For WIN the largest correlation was at lag +4 ($r = 0.5$) and for EIN at lag +5 ($r = 0.4$). After removing the BWA from WIN and EIN, the anticorrelation between them became

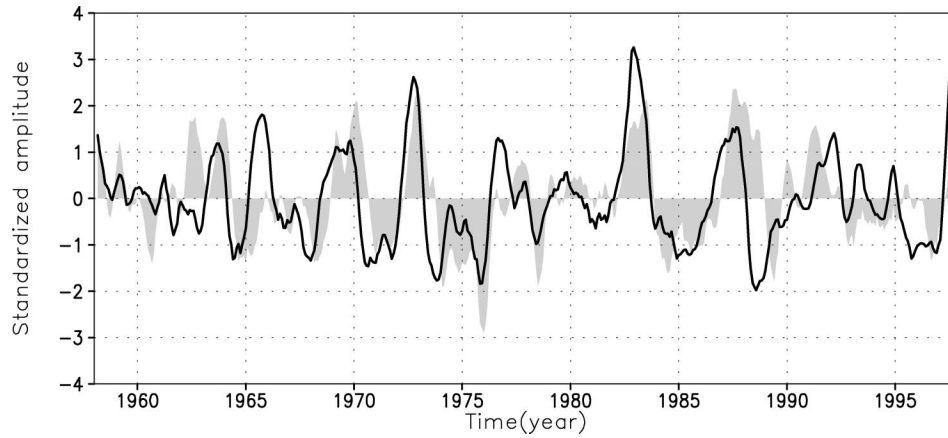


FIG. 6. The time series of monthly Niño-3 SSTA (solid line) and that of BWA (gray-filled shades). The BWA is the area-averaged SSTA from 20°S–20°N, 40°–100°E. Both time series were standardized by their respective std dev ($\sigma_{\text{Niño-3}} = 0.8$, $\sigma_{\text{BWA}} = 0.2$). A 5-month running mean filter was applied to both time series.

stronger ($r = -0.5$). We also note that the lagged anticorrelation between JJA EIN and SON WIN ($r = -0.6$) is even stronger.

5. A multivariate criteria to identify IOD events

It is of relevance to estimate the contribution of IOD events to SST variability in the TIO and to compare it with contributions from other factors such as BWA, interdecadal anomaly, and linear trend. Given that the TIO SSTA is influenced by multiple factors, we formulated the following data preprocessing to isolate IOD related variability. Multivariate criteria as described below are then used to identify the IOD events in the analysis period.

1) *Preprocessing of data.* WIN, EIN, and U_{eq} were first detrended. A 3-month running mean was then ap-

plied once over all the three time series to reduce the impact of intraseasonal fluctuations. Then we filtered out the interdecadal anomaly (periodicities longer than 7 yr). Thereafter, the BWA lagged effect was removed from WIN and EIN, as explained in section 4c.

2) *Identifying criteria.* DMI and U_{eq} were required to exceed 0.5σ in amplitude for at least 3 months. In addition we require that the SSTA in WIN and EIN should be of opposite sign and the magnitude should exceed 0.5σ for at least 3 months.

Using the above procedure we identified 9 positive (SSTA over EIN is cool) and 10 negative (SSTA over EIN is warm) IOD events. The duration and peak of each of these events is shown in Fig. 7. Assuming normal sampling variability, point and interval estimates of the population mean (Snedecor and Cochran 1968) of

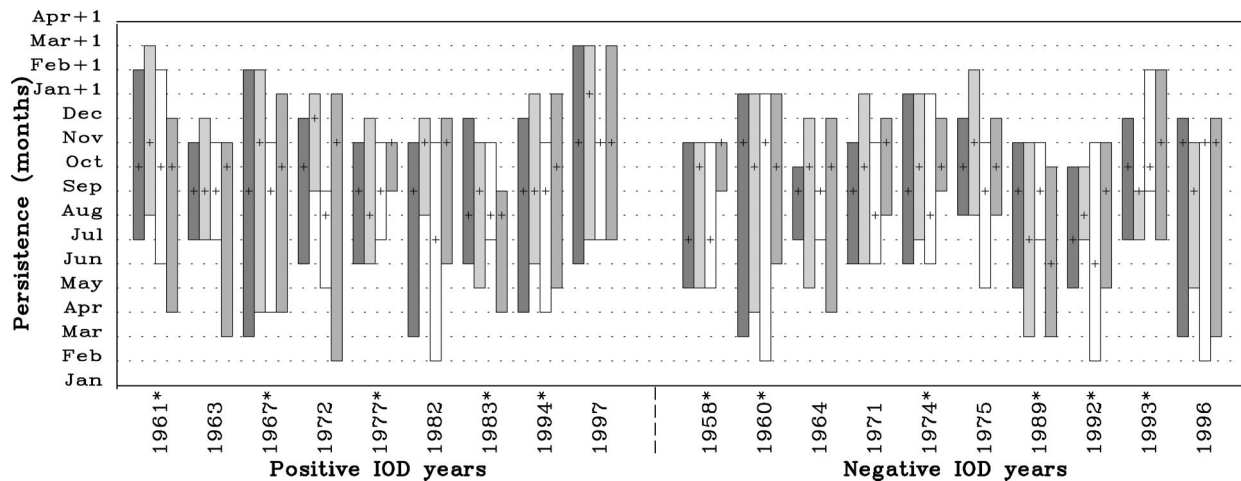


FIG. 7. The bars indicate the beginning, end, and duration of DMI (intermediate shade), WIN (outlined bar), EIN (lightest shade), and U_{eq} (darkest shade) during each of the 9 positive and 10 negative IOD years. The month of peak anomaly is indicated by a plus mark. Asterisk on the year indicates a pure IOD year (see text for definition).

the various statistics were calculated. We then defined a canonical IOD event in terms of the interval estimate of the population mean. A 95% confidence level based on the two-tailed t distribution is used.

A canonical IOD thus defined has the following properties. 1) Strongly anomalous DMI develops around boreal spring to early summer but vanishes after fall; peak DMI occurs in late summer or fall with anomalous activity prevailing for two to three seasons. 2) Anomalous WIN develops in boreal summer and lasts for two to three seasons before vanishing around late fall to winter; peak WIN anomaly occurs around fall. 3) Anomalous EIN develops around spring to early summer, lasts for two to three seasons, and vanishes around fall to winter with a peak around fall. 4) Anomalous U_{eq} develops around spring to early summer, and lasts for two to three seasons before vanishing around late fall to winter; anomalous U_{eq} peaks in the boreal fall.

We noted that both negative and positive IOD events in general have the same characteristics. Therefore, the above description may be applied to both phases. It should, however, be mentioned that negative IOD events have lesser amplitude compared to positive events, indicating a skewed distribution.

6. Relative contribution of IOD events to TIO variability

The collective contribution of these 19 IOD events to SST variability in the TIO was assessed. We first summed up the variance of SST over WIN and EIN only for those periods when the DMI was significantly anomalous (see Fig. 7). This calculation was performed using the reduced SST dataset, that is, the one filtered off the linear trend, the interdecadal anomaly, and the ENSO-lagged effect. The summed variance during IOD events was then compared to the total variance in the raw (or unfiltered) SST data.

The 19 events contribute about 23% (32%) to the total SSTA variance over WIN (EIN). However, the variance is unequally distributed over the seasons (Table 2). We note that it is in the summer and the fall seasons that the IOD events contribute strongly—27% (44%) of summer variability over WIN (EIN) and 37% (57%) of the fall variability over WIN (EIN).

The contribution of the trend, the interdecadal anomaly, and the BWA are also documented in Table 2 as a function of season. It is seen that on the interannual timescale (shorter than 7-yr period) IOD dominates SST variability over both WIN and EIN during the summer and fall seasons. On the other hand, the BWA predominates interannual variability during the boreal winter and spring seasons. The interdecadal timescale fluctuations are seen to have a significant contribution to SST variability over WIN and EIN in all the seasons. The linear trend is, on the other hand, strongest over WIN, contributing about 20% of the variability in most of the seasons.

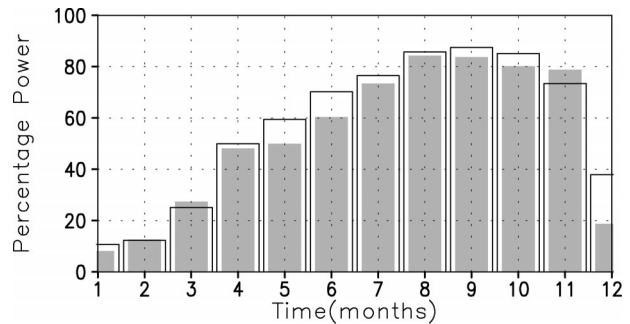


FIG. 8. Percentage of total variance for each month in the seasonal cycle contributed by the 19 IOD events identified in this study toward DMI (outlined bars) and U_{eq} (filled bars).

The IOD events appear to contribute strongly to DMI and U_{eq} variance. Both in DMI and U_{eq} , the IOD events accounted for nearly 70% of the total variability. However it is in the summer and fall seasons that the strongest variability of U_{eq} and DMI is manifested; most of this variance is associated with the 19 IOD events (Fig. 8).

7. Comparison of DMI and Niño-3 time series

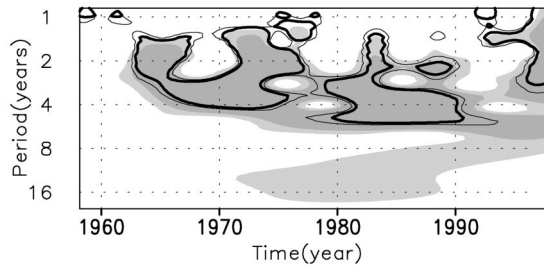
Performed over all months, the correlation between DMI and Niño-3 is weak ($r = 0.2$). However, when the data are seasonally stratified and the correlations calculated, significant correlation exists between DMI and Niño-3 at the 99% level during JJA and SON. The strongest simultaneous correlation exists during SON (Table 1).

However, even at the season of the strongest cross correlation, the variance of DMI associated with Niño-3 is less than 25%. This leads to two questions. (i) How similar are the time series of DMI and Niño-3? (ii) What factor(s) accounts for the rest of the variability in DMI not attributable to Niño-3?

To examine the extent to which these time series are similar, we have performed several analyses to be described below. To facilitate comparison, we will contrast the relation of DMI versus Niño-3 to that of BWA versus Niño-3. Note that BWA as introduced in section 4 represents the lagged cooling (warming) of the entire TIO following a La Niña (El Niño).

We start by examining the relation of both DMI and Niño-3 to BWA separately. The lag correlation for DMI versus BWA and Niño-3 versus BWA was computed with BWA lagging in both cases. To perform this calculation, we correlated the boreal fall (SON) value of DMI at a particular year with each month of the BWA time series in the following year. A similar correlation was performed for SON Niño-3 with monthly BWA. Niño-3 is significantly correlated with BWA up to 9-month lag with strongest correlation ($r > 0.6$) occurring in late winter/early spring season following ENSO. However, correlation between DMI and BWA is insignificant (close to 0.2) at all lags.

a. Wavelet spectrum for Niño3



b. Wavelet spectrum for BWA

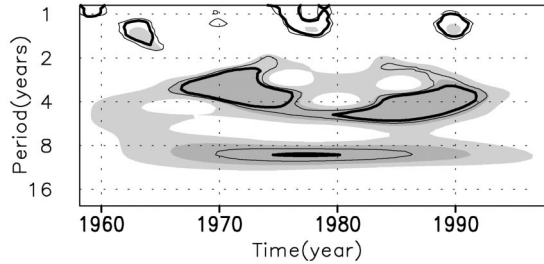


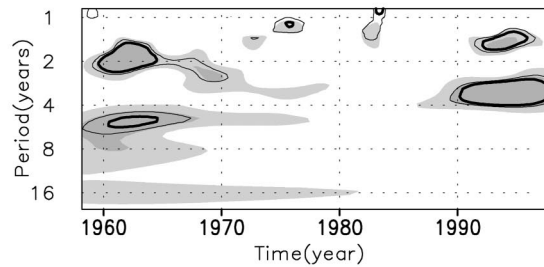
FIG. 9. The local wavelet power spectrum of (a) Niño-3 and (b) BWA using the Morlet wavelet. Shaded contours represent wavelet power standardized by the total power (integrated along wavelength and time) in the respective spectra. Light (darker) shading is power 2 (4) times above the total power. The thin (thick) contour encloses regions where statistical significance of the result exceeds 90% (95%) confidence level, estimated using Monte Carlo simulations.

Figure 9 shows the wavelet spectra of monthly Niño-3 and Fig. 10 that of monthly DMI using the Morlet wavelet (Torrence and Compo 1998). To test the significance of the local wavelet spectrum we performed Monte Carlo simulations using colored noise generated by a univariate lag-1 autoregressive [AR(1), or Markov] process acting on white noise. The synthetic time series was constructed to have the same lag-1 autocorrelation and variance as the observed time series being analyzed.

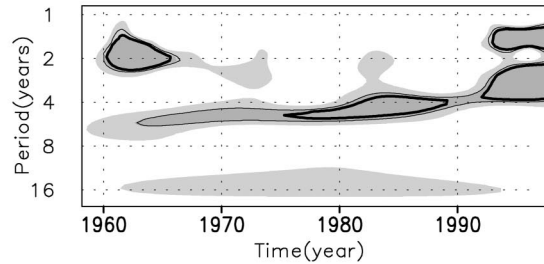
DMI and Niño-3 spectra have significant differences. Whereas the peak power in the Niño-3 spectrum is strongest in the 1970s and 1980s, the peak power in the DMI spectrum occurs during the early 1960s and the 1990s. The arclike curvature of the spectral peaks in the Niño-3 wavelet spectrum suggests a continual lengthening of the period of oscillation from the 1970s till the end of the 1980s. In the DMI spectrum, however, the spectral peaks appear to evolve with the same frequency during adjacent times.

The dissimilarity between wavelet spectra of DMI and Niño-3 may be contrasted with the similarity between those of Niño-3 and BWA. Both Niño-3 and BWA have strongest power in identical periods and identical bands. Further, the lengthening of the frequency noted in the Niño-3 spectrum is reflected in the BWA spectrum. It is to be noted, however, that interdecadal power in the

a. Wavelet spectrum for DMI



b. Wavelet spectrum for Ueq



c. Wavelet spectrum for reduced Ueq

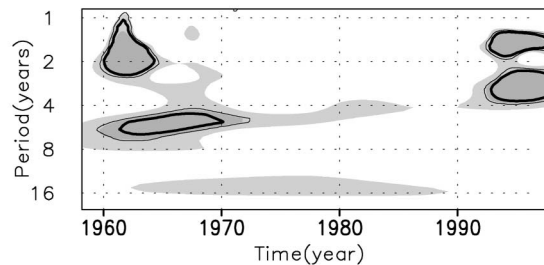
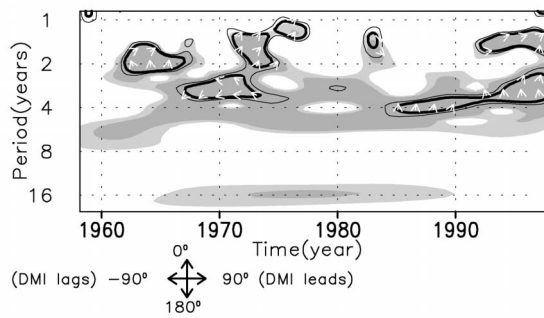


FIG. 10. Same as in Fig. 9, except the spectra are for (a) DMI, (b) U_{eq} , and (c) reduced U_{eq} .

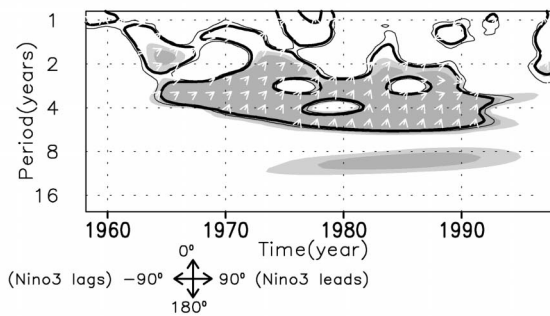
BWA appears not to be associated with that in the Niño-3 spectra.

These relationships can be quantitatively discussed by means of a cross-wavelet spectrum (Torrence and Compo 1998). The cross-wavelet spectra for DMI versus Niño-3 and Niño-3 versus BWA are plotted in Figs. 11a,b, respectively. Whereas cross-spectral power between Niño-3 and BWA is strong and significant at all the periodicities and time periods characteristic of Niño-3 activity, that between DMI and Niño-3 occurs only at certain time periods, which are a subset of the time periods of DMI activity (cf. Fig. 10). Here we note that the cross-wavelet results presented here and in section 8 are in good agreement with Ashok et al. (2003) who used wavelet coherence to explore the relation between IOD and ENSO. Consistent with other studies (e.g., Klein et al. 1999), the phase information in Fig. 11 suggests that BWA lags the Niño-3 time series by about a season or so. The phase between DMI and Niño-3,

a. Cross wavelet spectrum DMI vs. Niño3



b. Cross wavelet spectrum Niño3 vs. BWA



c. Cross wavelet spectrum DMI vs. Ueq

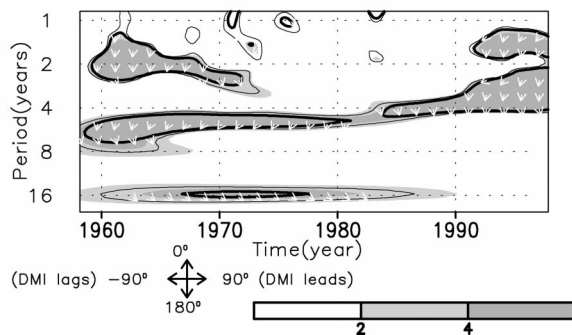


FIG. 11. The cross-wavelet spectrum of (a) DMI vs Niño-3, (b) Niño-3 vs BWA, and (c) DMI vs U_{eq} . Shaded contours represent cross-wavelet power standardized by the total power (integrated along wavelength and time) in the spectrum. Light (darker) shading is power 2 (4) times above total power. The thin (thick) contour encloses regions where the statistical significance of the result exceeds the 90% (95%) confidence level, determined through Monte Carlo simulations.

on the other hand, suggests concurrent activity during co-occurrence.

The scale averaged 2–7-yr wavelet variance time series in Fig. 12 shows significant interdecadal modulation of DMI (gray positive curve) and Niño-3 (thick dashed line) activity. For this calculation the unnormalized wavelet power spectrum was divided by its corresponding wavelets scale and the contributions from the 2–7-yr scales were summed up (Torrence and Compo 1998). In general, periods of high DMI activity appear to be accompanied by periods of low Niño-3 activity and vice versa. The correlation between the two scale-averaged

variance time series is -0.72 . On the other hand, the scale-averaged variance time series of BWA is positively correlated with that of Niño-3 ($r = +0.85$). It is noted that the longest decorrelation time among the 2–7-yr scale-averaged time series shown in Fig. 12 is 55 months, determined from the e -folding time. This yields 9 degrees of freedom. We note that the out-of-phase relation between power evolution of DMI and Niño-3 is significant at the 95% level, whereas the in-phase relation between Niño-3 and BWA is significant at the 99% level.

A series of composite analyses are presented in Figs. 13a–c. The dataset is divided into three categories: a) pure IOD events, b) pure ENSO events, and c) co-occurring IOD and ENSO events. Following Rao et al. (2002) a pure IOD event is one which occurred in the absence of an ENSO event. A positive IOD event that co-occurred with a La Niña (e.g., 1967) or a negative IOD event that co-occurred with an El Niño (e.g., 1958) is also considered a pure IOD event. A pure ENSO event is similarly defined. In this paper we adopted the Japanese Meteorological Agency (JMA) definition of ENSO (see Trenberth 1997): those events where the 5-month running mean averaged Niño-3 index exceeded 0.5°C for six consecutive months.

In the period 1958–97, 11 out of the 19 IOD events are pure IOD events. Collectively they account for 43% of DMI variability, but only 7% of Niño-3 variability. Out of this, the largest fraction (2.2%) was contributed by the La Niña of 1967, which occurred along with a positive IOD event. The eight IOD events that co-occurred with ENSO contributed 26% to the DMI variability, while the associated Niño-3 variability was 36%.

From the three sets of composite maps in Fig. 13, a few points are noted. IOD activity occurs both in the presence and absence of ENSO activity; the strength of IOD activity is almost the same both in the absence and presence of ENSO. ENSO activity occurs both in the presence and absence of IOD. However, stronger ENSO activity is apparent in the composites of ENSO events that co-occurred with IOD events. Though IOD activity is essentially unchanged whether or not it occurred with an ENSO, a few subtle but significant differences are apparent when an IOD co-occurs with an ENSO: a) the SSTA over WIN is stronger; b) the SSTA over EIN is weaker; and c) the zonal wind anomaly U_{eq} is stronger.

In summary, the above observations are inconsistent with the hypothesis that the correlation between DMI and Niño-3 implicate IOD as a part of ENSO evolution in the TIO (Nicholls and Drosowsky 2001; Baquero-Bernal and Latif 2002; Hendon 2003). On the other hand, our results do suggest that a large part of the positive correlation is probably due to the co-occurrence of a few strong ENSO events with strong IOD events. The following calculation appears to verify it. We removed four strong co-occurring events—those of 1997, 1982, 1972, and 1963—from both the DMI and Niño-3 time series. This removal resulted in a 44% reduction

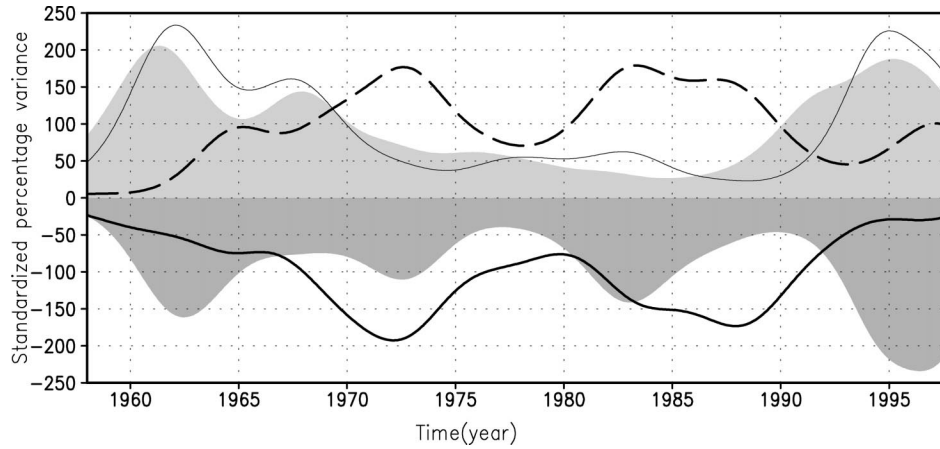


FIG. 12. The scale-averaged wavelet power over the 2–7-yr band for DMI (light gray shades), U_{eq} (dark gray shades), reduced U_{eq} (solid thin line), Niño-3 (dashed thick line), and BWA (solid thick line). The signs of scale-averaged power for U_{eq} and BWA are inverted. All the variables were divided by the average of their respective power over the 40-yr period and multiplied by 100.

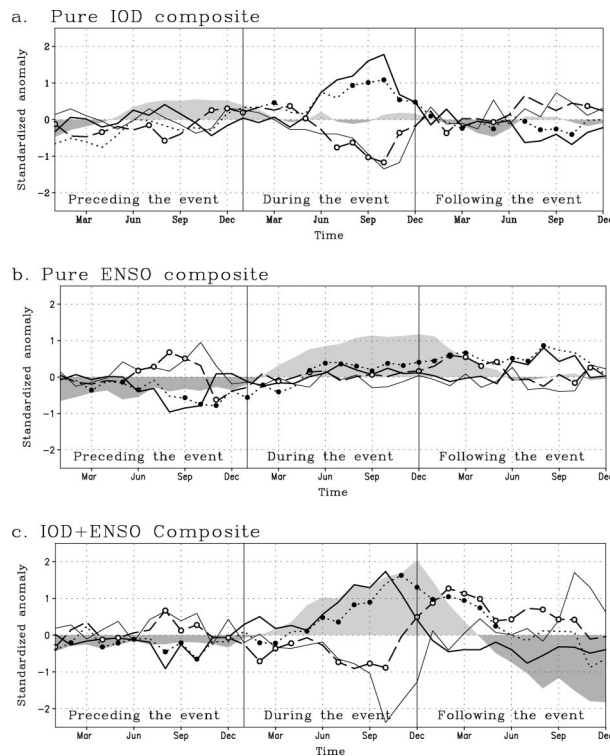


FIG. 13. Composite map of DMI (thick solid line), U_{eq} (thin solid line), WIN (thick dotted line), EIN (thick dashed line), and Niño-3 (gray-filled line) anomalies for three categories: (a) pure IOD events (1961, 1967, 1977, 1983, 1994, 1958, 1960, 1974, 1989, 1992, 1993), (b) pure ENSO events (1965, 1969, 1976, 1986, 1987, 1967, 1970, 1973, 1978, 1984, 1985, 1988), and (c) co-occurring IOD + ENSO events (1963, 1972, 1982, 1997, 1964, 1971, 1975, 1996). Negative IOD years and La Niña years are in italics. Composite includes both phases of the IOD and ENSO events. All variables are standardized for plotting convenience. The open (closed) circles on EIN (WIN) indicate significance at the 95% level based on two-tailed t test, except for (c) where the test is passed only at the 90% level.

of variance in the Niño-3 time series. In contrast, the DMI time series retained up to 83% of its variance. Upon recalculating the correlation between SON DMI and Niño-3 (Table 3), we found that it was insignificant ($r = 0.23$) at even the 90% level.

8. Comparison of DMI and U_{eq} time series

This leads to the next question: what factor(s) accounts for the rest of the variability in DMI not attributable to Niño-3?

From Table 2, it is seen that the strongest correlation of DMI is with U_{eq} in SON at $r = -0.85$. Thus, U_{eq} is associated with about 70% of the variance in DMI in contrast to the 25% explained by Niño-3. In contrast to Niño-3, whose association with DMI is insignificant when all the months are considered, the association of DMI and U_{eq} is significant (at the 99% level; $r = -0.5$) even if considered over all months. We also note that if we remove the four years 1997, 1982, 1972, and 1963 and recalculate r between DMI and U_{eq} for SON (Table 3), the correlation is still highly significant at $r = -0.82$. However, due to this operation, U_{eq} loses about 34% of its variance. The larger loss of variance in U_{eq} compared to that in DMI is presumably because significant equatorial wind anomalies are also forced by the ENSO during SON (Feng and Meyers 2003; also see Table 1 and Fig. 14). In the rest of this section, we further explore the similarity between DMI and U_{eq} , keeping in mind that U_{eq} can also be partially induced by ENSO-related atmospheric processes (Hendon 2003).

Figure 10 shows the wavelet spectra of monthly DMI and U_{eq} . Both appear to have similar frequency content during corresponding time periods: a distinct biennial periodicity in the 1960s, and a quasi-triennial periodicity in the 1990s superimposed on a nearly biennial periodicity visibly separated from it. In the intervening pe-

TABLE 2. Percent variance contributed by the linear trend, the interdecadal anomaly, the BWA, and IOD to the SST variability over WIN and EIN.

	WIN				EIN			
	MAM	JJA	SON	DJF	MAM	JJA	SON	DJF
Trend	22%	21%	19%	7%	8%	4%	12%	6%
Interdecadal anomaly	29%	10%	14%	31%	34%	29%	29%	17%
BWA	31%	14%	20%	37%	30%	8%	3%	25%
IOD	7%	27%	37%	18%	11%	44%	57%	8%

riod between the 1970s and the 1990s there is weak activity in both DMI and U_{eq} that is indistinguishable from noise. A noticeable difference is that U_{eq} has significant fluctuations in a quadrennial band during the late 1970s and the 1980s. It is also noted that DMI has a quasi-pentadal variability in the 1960s that appears to be weaker in U_{eq} .

Some of the characteristics of the U_{eq} spectrum not related to DMI appear to have been introduced by ENSO. To demonstrate this, we removed the partial influence of Niño-3 on U_{eq} . To do this, we use a multiple regression formulation with U_{eq} as the dependent variable and Niño-3 and DMI as independent variables. The partial correlation (Cohen and Cohen 1983) of DMI on U_{eq} after partialling the effect of Niño-3 is given by

$$r_{1y,2} = \frac{r_{1y} - r_{2y}r_{12}}{\sqrt{(1 - r_{12}^2)(1 - r_{2y}^2)}}, \quad (1)$$

where r_{1y} is the simple correlation of U_{eq} with DMI, r_{2y} that of U_{eq} with Niño-3, and r_{12} that of DMI with Niño-3. Similarly $r_{2y,1}$ is the partial correlation of Niño-3 on U_{eq} after partialling the effect of DMI. Hereafter we will refer to the U_{eq} filtered off the Niño-3 contribution as reduced U_{eq} . It is noted that the wavelet spectrum of reduced U_{eq} shown in Fig. 10c bears closer resemblance to the DMI spectrum than the total U_{eq} (Fig. 10b).

The wavelet cross-spectrum (Torrence and Compo 1998) for DMI versus total U_{eq} shown in Fig. 11c shows significant covariability in all the time periods and frequency bands characteristic of DMI (cf. Fig. 10a). At all times and periods of high DMI activity, DMI and U_{eq} have an out-of-phase relation. Interestingly, strong covariance is also noted in a very low-frequency band

with 16-yr periodicity where DMI leads U_{eq} by about one quarter of a cycle (about 4 yr).

The 2–7-yr scale-averaged variance time series (Fig. 12) reveals periods of high DMI activity accompanied by periods of high total U_{eq} activity and vice versa, though the correspondence between total U_{eq} and DMI is not perfect ($r = 0.5$; not significant at the 95% level). However, the correlation is significant at the 99% level ($r = 0.88$) between scale-averaged variance time series of reduced U_{eq} (thin solid line in Fig. 12) and DMI.

9. Discussion

The nature of SSTA variability related to IOD has been much debated (e.g., Dommenget and Latif 2002; Behera et al. 2003). Our analyses show that during IOD events, surface zonal wind anomalies over the equatorial Indian Ocean are associated with an out-of-phase SSTA pattern that is most prominent in the boreal fall. Composite analysis of SSTA during IOD events presented here as well as in other studies (S99; Rao et al. 2002) and case studies of individual events (Reverdin et al. 1986; Webster et al. 1999; Murtugudde et al. 2000; Feng and Meyers 2003) supports this inference. Ocean modeling studies (Behera et al. 1999; Murtugudde et al. 2000; Vinayachandran et al. 2002) suggest that such an SSTA pattern is potentially forced by the equatorial wind stress through excitement of oceanic planetary and Kelvin waves and the consequent modulation of entrainment and advective transports. The wind may also act by modulating thermodynamic fluxes (Behera et al. 1999; Yu and Rienecker 1999). It is noteworthy that the presence of such large-scale oceanic waves have been observed in the TIO during the recent IOD events of 1994 and 1997 (Behera et al. 1999; Webster et al. 1999; Rao et al. 2002; Feng and Meyers 2003). Taken together, these diverse pieces of information favor the reality of the dipolelike SSTA pattern.

Our analyses suggest that the nonstationarity of the mean SST may be largely to blame in the masking of the anticorrelation implicit in the IOD SSTA pattern. In particular, around the time of the so-called regime shift (Nitta and Yamada 1989) and accelerated warming stronger than the linear trend is seen over both WIN and EIN. We also noted that it is in this latter period that the anticorrelation is suppressed. For example, cor-

TABLE 3. Cross-correlation matrix for WIN, EIN, DMI, U_{eq} , and Niño-3 after removing the years 1963, 1972, 1982, and 1997. Correlations significant at the 99% level are bold. The data was detrended and the decadal anomaly removed before calculating the correlation coefficients.

	Category				
	WIN	EIN	DMI	U_{eq}	Niño-3
WIN		-0.5	0.70	-0.51	0.01
EIN			-0.83	0.78	-0.26
DMI				-0.82	0.23
U_{eq}					-0.27

relation between WIN and EIN for the 20-yr period from 1958 to 1977 is highly significant and negative ($r = -0.5$) even in unfiltered data. On the other hand, in the latter part of the period from 1978 to 1997 WIN and EIN have insignificant correlation. The filtering of the interdecadal anomaly appears to affect this latter period most; correlation between WIN and EIN for 1978–97 after removing the interdecadal anomaly is $r = -0.32$.

We find little evidence for the hypothesis that the IOD phenomenon is a part of the ENSO. Though IOD and ENSO indices are significantly correlated during boreal fall, the shared variance is moderate. Further time-evolution spectra of DMI and Niño-3 are significantly different. We also showed that DMI variance is generally strong during weak ENSO activity and vice versa. Interestingly, coral-derived proxy SSTA records show that IOD activity is significantly higher in the Holocene, which is generally agreed upon to be a time of weak ENSO activity (Abram et al. 2001). These analyses suggest that IOD cannot be described as a function of ENSO. Further, as shown here, the strength of the association between ENSO and IOD can be largely attributed to the co-occurrence of a few strong IOD and ENSO events. ENSO events occurring during co-occurrences are amplified relative to pure ENSO events and such events contribute a disproportionately large amount of ENSO variability. In contrast, most of the variance of IOD events occurs from pure IOD events. It is noteworthy that the correlation between DMI and Niño-3 is insignificant during SON if we remove the events of 1997, 1982, 1972, and 1963 from the calculation. Though this removal resulted in nearly half of the Niño-3 variance being reduced, the DMI time series retained more than 80% of its variance.

On the other hand, oceanic variability within the TIO is more strongly correlated with atmospheric variability within the TIO (section 8). Further, DMI and U_{eq} spectra are remarkably similar. The interdecadal modulation of power in both are also similar if a partial ENSO effect on the surface wind is removed. These observations indicate a possibility for the IOD arising out coupled ocean–atmospheric instabilities within the TIO. The simulation of realistic and energetic IOD events in a high-resolution coupled GCM with weak ENSO activity (Iizuka et al. 2000) appears to support this possibility.

However, it is important to distinguish that while our results indicate an inherent mode of TIO variability, we cannot resolve on the basis of this analysis alone whether IOD sustains itself or whether it is a damped mode requiring an external trigger. One cannot rule out the possibility that the air–sea interactions giving rise to IOD may be triggered by ENSO (Ueda and Matsumoto 2000; Annamalai et al. 2003) during certain years or by intraseasonal oscillations (Li et al. 2003; Wang et al. 2002, manuscript submitted to *J. Climate*) within the TIO during other years. The near-simultaneous development of both IOD and ENSO implies a limitation in exploring this possibility using conventional data. Rel-

atively high temporally resolved data or suitably designed coupled model experiments are needed to address these possibilities.

It is remarkable that there is strong systematic behavior in the phase of IOD and ENSO events. We note that, in general, positive IOD events have a tendency to co-occur with El Niños and negative IODs with La Niñas. We do also note that in the 40-yr time period that we analyzed, ENSO events that co-occurred with IOD events are stronger than pure ENSO events. Though IOD events appear to be equally strong whether or not it co-occurred with ENSO, two notable exceptions are as follows: (i) the zonal wind field over the equator is significantly stronger during co-occurrences and (ii) the IOD SST pattern appears to be overlaid by a basin-wide uniform anomaly.

A possible hypothesis that may explain the systematic behavior between IOD and ENSO is suggested through the multiple regression analysis presented in Fig. 14. In Figs. 14a–d we have correlated tropical Indo-Pacific SSTA on U_{eq} , an IOD index, after partialling out the possible influence of ENSO [see Eq. (1)]. We then correlated surface wind anomalies on DMI, another IOD index, after partialling out the possible influence of ENSO. The U_{eq} was used in finding the SSTA structure instead of DMI, since the use of DMI would, by its construction, introduce an artificial dipole SSTA pattern over the TIO. Similarly, the SSTA and wind pattern associated with ENSO (Figs. 14e–h) can be found by correlating these fields with Niño-3 after partialling the effect of IOD. These figures indicate a significant potential in both phenomena to influence each other. For example, in the case of IOD we note that during boreal summer (fall) westerly winds associated with it extend up to (beyond) the date line. The structure of the wind anomaly and its eastward-propagating character suggests the presence of the atmospheric Kelvin wave. It is possible that these westerly winds sitting over the equatorial west Pacific may trigger an ENSO or strengthen an existing one.

A case in point may be the ephemeral El Niño during the year 1994. We note that the beginning of the year 1994 was characterized by La Niña conditions. By August, however, the La Niña gave way to a weak El Niño, a time at which the IOD was fully developed. We speculate that this reversal may have been brought about by westerly wind anomalies induced over the western Pacific by the strong IOD event of 1994.

Similarly, in the case of the ENSO (Figs. 14e–h), easterly winds are seen extending over the eastern equatorial Indian Ocean during boreal fall. These are capable of positively influencing an IOD event by upwelling more cold water off Sumatra and thereby enhancing the SSTA. The phase of the wind anomaly over the TIO during ENSO also suggests that an IOD phase not consistent the ENSO phase may be dampened. This implies that positive IOD conditions could be suppressed during

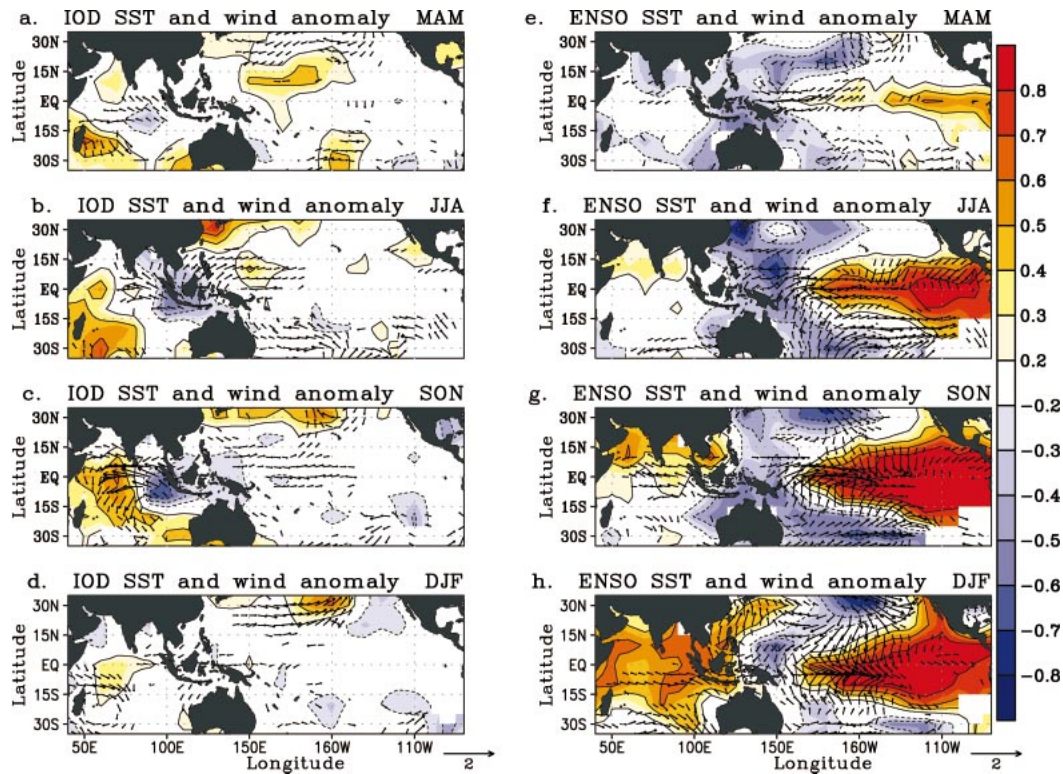


FIG. 14. (a)–(d) The partial correlation of SST (shaded contours) on U_{eq} (SON) and the partial regression of surface winds on DMI (SON), after accounting for the effect of Niño-3. Wind vectors of magnitude smaller than 0.2 m s^{-1} are not plotted. For purposes of plotting, the original $10^\circ \times 10^\circ$ grid was interpolated to a $5^\circ \times 5^\circ$ grid. (e)–(h) The same as in (a)–(d) but for the partial correlation and the partial regression of SST and winds, respectively, on Niño-3 after accounting for the effect of DMI.

a La Niña, but supported and amplified during an El Niño.

The analysis also suggests that the largest ENSO effect on TIO SST may be the lagged effect or the BWA. Some recent (Hendon 2003; Alexander et al. 2002; Xie et al. 2002) and previous (Hastenrath et al. 1993) studies suggest that an SST structure similar to the IOD pattern is manifested in the TIO during SON. In contrast, the composites of pure ENSO events in Fig. 13b, as well as the partial correlation analysis presented in Figs. 14e–h suggest that ENSO events have hardly any simultaneous impacts over WIN and EIN during JJA or SON. Three of the findings reported in this study can be used to explain this discrepancy: (i) ENSO events that co-occur with IOD are stronger than pure ENSOs; (ii) IOD events that do and do not co-occur with ENSOs have the same amplitude; and (iii) there is a systematic tendency for a positive (negative) IOD to co-occur with El Niño (La Niña). Consequently, simple regression analysis, which highlights large-amplitude events or composite analysis with all ENSO events, portrays a mixture of responses to an IOD event and an ENSO event rather than the pure response to ENSO.

Though this analysis rules out a significant response by ENSO over WIN and EIN during JJA and SON, it should not be interpreted to mean that simultaneous

ENSO response in the TIO is negligible. As seen in Fig. 14, ENSO has a significant response over both the western and eastern TIO; however, these regions of ENSO influence are quite distinct from regions affected by IOD. The most fundamental difference between the two patterns in the eastern TIO is that SSTA associated with IOD is trapped to the Indonesian coast line while that associated with ENSO is trapped to the Australian coast line. These distinct SSTA structures are indeed a reflection of coastally trapped Kelvin wave–induced thermocline changes along the Indonesian waveguide and the Australian waveguide, respectively (Meyers 1996). Modeling (Vinayachandran et al. 1999; Behera et al. 1999; Murtugudde et al. 2000) and observational (Rao et al. 2002; Feng and Meyers 2003) studies demonstrate that the IOD SSTA pattern off Java is a consequence of Kelvin waves striking the Indonesian coast at the equator and, consequently, traveling along the Indonesian waveguide as a coastally trapped Kelvin wave. Other modeling (Clarke and Liu 1994; Verschell et al. 1995) and observational studies (Meyers 1996) have shown that western Pacific sea level anomaly during ENSO resulting from the arrival of Rossby waves is transmitted into the TIO through the junction of the Pacific equatorial waveguide with the Papua New Guinea–western Australia waveguide northwest of Papua New Guinea.

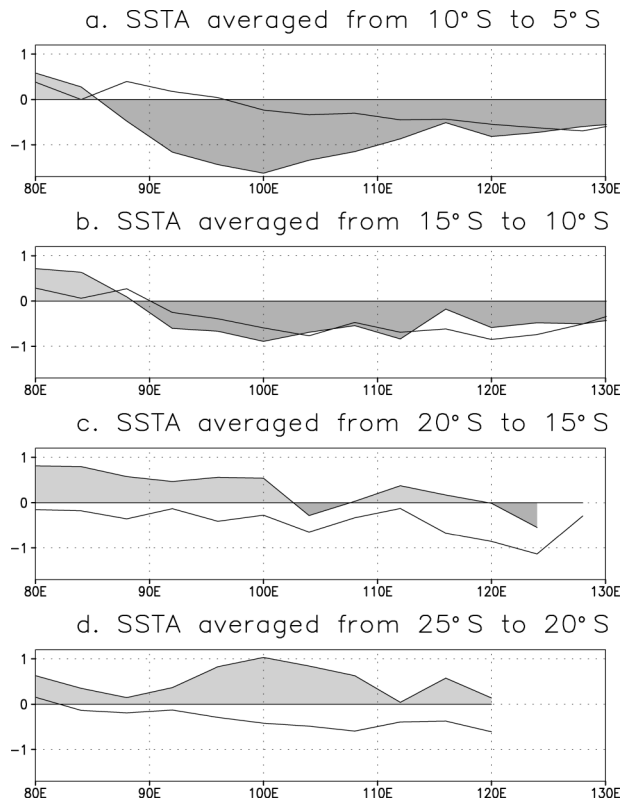


FIG. 15. Longitudinal section of composite SST anomaly at the eastern TIO associated with pure IOD (gray-filled line) and pure ENSO events (solid line) averaged over various latitudinal bands. The SST anomaly is standardized by the area-averaged anomaly over EIN.

The ENSO SSTA pattern shown in Fig. 14 over the eastern TIO is consistent with this coastal waveguide paradigm (S. Wijffels and G. Meyers 2003, personal communication).

Finally, we note that the physical proximity of the ENSO and IOD signals in the eastern TIO pose a practical problem in defining EIN. To illustrate this we have shown in Fig. 15 the SSTA response to pure IOD and pure ENSO events at various latitude bands south of the equator. All of the anomalies are normalized by the anomaly over EIN to bring out their magnitude relative to EIN. Over EIN, the ENSO signal has negligible magnitude while the IOD signal has maximum magnitude. In agreement with the multiple regression analysis presented in Fig. 14, it is seen that the ENSO signal is trapped to the Australian coast with maximum anomaly around 15°–20°S and 125°E. Similarly in agreement with Fig. 14, it is seen that the IOD SSTA signal goes from cold anomaly north of 15°S to warm anomaly south of that. Therefore, as one moves away either east or south of EIN, the IOD signal weakens relative to the ENSO signal. For example, at 10°S and 115°E, the ENSO signal is as strong as the IOD signal and strengthens to the east of this point. Also, south of 10°S the ENSO signal relatively strengthens compared to the

IOD signal. Thus, although the IOD signal does extend to the east and south of 110°E and 10°S, we have restricted our definition of EIN to be a box between 10°S–0° and 90°–110°E, so as to avoid the obvious contamination of the IOD by the ENSO signal.

10. Summary

SST and surface wind observations in the TIO were analyzed for the 40 years from 1958 to 1997 and the following results were found.

- 1) SST variability has a complex nature and appears to be somewhat equally contributed by linear trend, interdecadal anomaly, the lagged effect of ENSO and IOD.
- 2) The correlation between WIN and EIN becomes highly significant and negative only if the interdecadal anomaly is removed, though there is a suggestion that this is mostly true only for the latter half of the record, when there is a rapid warming of the mean SST in both the western and eastern TIO.
- 3) Though IOD is only one of the several factors shaping SSTA in the TIO, its influence appears to be substantial in the zonal SST gradient and surface wind anomaly. The surface wind anomaly is, to a lesser extent, also affected by ENSO.
- 4) IOD events do frequently occur independent of ENSO activity. In this study, 11 such IOD events were identified. The predominant proportion of IOD variance comes from these independent events: for instance, 43% of the DMI variance by the 11 independent events, compared to 26% variance carried by the 8 that co-occurred with ENSO. Conversely, Niño-3 activity during the 11 independent events was 7% of the total Niño-3 variance.
- 5) The highly significant correlation between DMI and Niño-3 during SON becomes insignificant even at the 90% level if the four events of 1997, 1982, 1972, and 1963 are removed from the correlation analysis.
- 6) The wavelet spectra of DMI and Niño-3 indices show significant differences. On the other hand, DMI and U_{eq} indices are quite similar. ENSO activity appears to be weaker during times of high IOD variance and vice versa.

Acknowledgments. We thank Drs. Shang Ping Xie, Bhupendra Nath Goswami, and Gary Meyers for their invaluable comments and discussions. Incisive yet instructive comments by Dr. Tommy Jensen and an anonymous referee have significantly improved the manuscript. COADS data were provided by Dr. Steve Worley of NCAR. The wavelet software was provided by C. Torrence and G. Compo and is available online at <http://paos.colorado.edu/research/wavelets/>. A pseudorandom number generator, the Mersene Twister, developed by M. Matsumoto and T. Nishimura, was used for the Monte Carlo simulations and is available online at <http://>

www.math.keio.ac.jp/matumoto/emt.html. Part of the work was completed at the International Pacific Research Center (IPRC). The IPRC is supported in part by the Frontier Research System for Global Change.

REFERENCES

- Abram, N. J., M. K. Gagan, W. S. Hantoro, M. T. McCulloh, and J. Chappell, 2001: Coral records of the Indian Ocean Dipole. *Eos, Trans. Amer. Geophys. Union*, **82**, Abstract PP11A-0443.
- Alexander, M. A., I. Blade, M. Newman, J. R. Lazante, N.-C. Lau, and J. D. Scott, 2002: The atmospheric bridge: The influence of ENSO teleconnections on air–sea interaction over the global Oceans. *J. Climate*, **15**, 2205–2231.
- Annamalai, H., R. Murtugudde, J. Potemra, S. Xie, P. Liu, and B. Wang, 2003: Coupled dynamics over the Indian Ocean: Spring initiation of the zonal mode. *Deep-Sea Res.*, in press.
- Ashok, K., Z. Guan, and T. Yamagata, 2001: Impact of the Indian Ocean Dipole on the relationship between the Indian monsoon rainfall and ENSO. *Geophys. Res. Lett.*, **28**, 4499–4502.
- , —, and —, 2003: A look at the relationship between the ENSO and the Indian Ocean Dipole. *J. Meteor. Soc. Japan*, **81**, 41–56.
- Baquero-Bernal, A., and M. Latif, 2002: On dipole-like variability in the tropical Indian Ocean. *J. Climate*, **15**, 1358–1368.
- Behera, S. K., and T. Yamagata, 2003: Impact of the Indian Ocean Dipole on the Southern Oscillation. *J. Meteor. Soc. Japan*, **81**, 169–177.
- , S. Krishnan, and T. Yamagata, 1999: Anomalous air–sea coupling in the southern tropical Indian Ocean during the boreal summer of 1994. *Geophys. Res. Lett.*, **26**, 3001–3004.
- , A. S. Rao, S. N. Hameed, and T. Yamagata, 2003: Comments on “A cautionary note on the interpretation of EOFs.” *J. Climate*, **16**, 1087–1093.
- Cadet, D. L., 1985: The Southern Oscillation over the Indian Ocean. *J. Climatol.*, **5**, 189–212.
- Chambers, D. P., B. D. Tapley, and R. H. Stewart, 1999: Anomalous warming in the Indian Ocean coincident with El Niño. *J. Geophys. Res.*, **104**, 10 525–10 533.
- Clark, C. O., P. J. Webster, and J. E. Cole, 2003: Interdecadal variability of the relationship between the Indian Ocean Zonal Mode and East African coastal rainfall anomalies. *J. Climate*, **16**, 548–554.
- Clarke, A. J., and X. Liu, 1994: Interannual sea level in the northern and eastern Indian Ocean. *J. Phys. Oceanogr.*, **24**, 1224–1235.
- , and A. Lebedev, 1997: Interannual and decadal changes in equatorial wind stress in the Atlantic, Indian, and Pacific Oceans and the eastern coastal response. *J. Climate*, **10**, 1722–1729.
- Cohen, J., and P. Cohen, 1983: *Applied Multiple Regression/Correlation Analysis for the Behavioral Sciences*. Lawrence Erlbaum Associates, 545 pp.
- Dommenget, D., and M. Latif, 2002: A cautionary note on the interpretation of EOFs. *J. Climate*, **15**, 216–225.
- Enfield, D. B., and A. M. Mestas-Nunez, 2000: Global modes of ENSO and non-ENSO SST variability and their associations with climate. *El Niño and the Southern Oscillation: Multiscale Variability and Global and Regional Impacts*, H. F. Diaz and V. Markgraf, Eds., Cambridge University Press, 89–112.
- Feng, M., and G. Meyers, 2003: Interannual variability in the tropical Indian Ocean: A two-year time scale of IOD. *Deep-Sea Res.*, in press.
- , —, and S. Wijffels, 2001: Interannual upper ocean variability in the tropical Indian Ocean. *Geophys. Res. Lett.*, **28**, 4151–4154.
- Flohn, H., 1987: East African rains of 1961/62 and the abrupt change of the White Nile discharge. *Palaeoecol. Afr.*, **18**, 3–18.
- Hastenrath, S., 2002: Dipoles, temperature gradients and tropical climate anomalies. *Bull. Amer. Meteor. Soc.*, **83**, 735–738.
- , A. Nicklis, and L. Greischar, 1993: Atmospheric–hydrospheric mechanisms of climate anomalies in the western equatorial Indian Ocean. *J. Geophys. Res.*, **98**, 20 219–20 235.
- Hendon, H. H., 2003: Indonesian rainfall variability: Impacts of ENSO and local air–sea interaction. *J. Climate*, **16**, 1775–1790.
- Iizuka, S., T. Matsuura, and T. Yamagata, 2000: The Indian Ocean SST dipole simulated in a coupled general circulation model. *Geophys. Res. Lett.*, **27**, 3369–3372.
- Kaplan, A., M. Cane, Y. Kushnir, A. Clement, M. Blumenthal, and B. Rajagopalan, 1998: Analysis of global sea surface temperature 1856–1991. *J. Geophys. Res.*, **103**, 18 567–18 589.
- Klein, S. A., B. J. Soden, and N. C. Lau, 1999: Remote sea surface temperature variations during ENSO: Evidence for a tropical atmospheric bridge. *J. Climate*, **12**, 917–932.
- Li, T., Y. Zhang, E. Lu, and D. Wang, 2002: Relative role of dynamic and thermodynamic processes in the development of the Indian Ocean dipole: An OGCM diagnosis. *Geophys. Res. Lett.*, **29**, 2110, doi:10.1029/2002GL015789.
- , B. Wang, C.-P. Chang, and Y. S. Zhang, 2003: A theory for the Indian Ocean dipole–zonal mode. *J. Atmos. Sci.*, **60**, 2119–2135.
- Meyers, G., 1996: Variation of Indonesian throughflow and the El Niño–Southern Oscillation. *J. Geophys. Res.*, **101**, 12 255–12 263.
- Murtugudde, R. G., J. P. McCreary, and A. J. Busalacchi, 2000: Oceanic processes associated with anomalous events in the Indian Ocean with relevance to 1997–1998. *J. Geophys. Res.*, **105**, 3295–3306.
- Nicholls, N., 1989: Sea surface temperatures and Australian winter rainfall. *J. Climate*, **2**, 965–973.
- , and W. Drosowsky, 2001: Is there an equatorial Indian Ocean dipole, independent of the El Niño–Southern Oscillation? *Extended Abstracts, Symp. on Climate Variability, the Oceans, and Societal Impacts*, Albuquerque, NM, Amer. Meteor. Soc., 17–18.
- Nitta, T., and S. Yamada, 1989: Recent warming of tropical sea surface temperature and its relationship to the Northern Hemisphere circulation. *J. Meteor. Soc. Japan*, **67**, 375–383.
- Rao, A. S., S. K. Behera, Y. Masumoto, and T. Yamagata, 2002: Interannual variability in the subsurface tropical Indian Ocean. *Deep-Sea Res.*, **49B**, 1549–1572.
- Rayner, N. A., E. B. Horton, D. E. Parker, C. K. Folland, and R. B. Hackett, 1996: Version 2.2 of the Global Sea-Ice and Sea Surface Temperature Data Set, 1903–1994. Hadley Centre for Climate Prediction and Research Tech. Rep., CRTN 74, U.K. Meteorological Office, Bracknell, United Kingdom, 35 pp.
- Reppin, J., F. A. Schott, J. Fischer, and D. Quadfasel, 1999: Equatorial currents and transports in the upper central Indian Ocean: Annual cycle and interannual variability. *J. Geophys. Res.*, **104**, 15 495–15 514.
- Reverdin, G., D. L. Cadet, and D. Gutzler, 1986: Interannual displacements of convection and surface circulation over the equatorial Indian Ocean. *Quart. J. Roy. Meteor. Soc.*, **112**, 43–67.
- Royer, T. C., 1989: Upper ocean temperature variability in the North-east Pacific Ocean: Is it an indicator of global warming? *J. Geophys. Res.*, **94**, 18 175–18 183.
- Saji, N. H., B. N. Goswami, P. N. Vinayachandran, and T. Yamagata, 1999: A dipole mode in the tropical Indian Ocean. *Nature*, **401**, 360–363.
- Schott, F., and J. P. McCreary, 2001: The monsoon circulation of the Indian Ocean. *Progress in Oceanography*, Vol. 51, Pergamon Press, 1–123.
- Snedecor, G. W., and W. Cochran, 1968: *Statistical Methods*. Iowa State University Press, 593 pp.
- Torrence, C., and G. P. Compo, 1998: A practical guide to wavelet analysis. *Bull. Amer. Meteor. Soc.*, **79**, 61–78.
- Trenberth, K. E., 1990: Recent observed interdecadal climate changes in the Northern Hemisphere. *Bull. Amer. Meteor. Soc.*, **71**, 988–993.
- , 1997: The definition of El Niño. *Bull. Amer. Meteor. Soc.*, **78**, 2771–2777.

- Ueda, H., and J. Matsumoto, 2000: A possible triggering process of east–west asymmetric anomalies over the Indian Ocean in relation to 1997/98 El Niño. *J. Meteor. Soc. Japan*, **78**, 803–818.
- Verschell, M. A., J. C. Kindle, and J. J. O'Brien, 1995: Effects of Indo-Pacific throughflow on the upper tropical Pacific and Indian Oceans. *J. Geophys. Res.*, **100**, 18 409–18 420.
- Vinayachandran, P. N., N. H. Saji, and T. Yamagata, 1999: Response of the equatorial Indian Ocean to an unusual wind event during 1994. *Geophys. Res. Lett.*, **26**, 1613–1616.
- , S. Iizuka, and T. Yamagata, 2002: Indian Ocean dipole mode events in an ocean general circulation model. *Deep-Sea Res.*, **49B**, 1573–1596.
- von Storch, H., and F. Zwiers, 1999: *Statistical Analysis in Climate Research*. Cambridge University Press, 484 pp.
- Wallace, J. M., E. M. Rasmusson, T. P. Mitchell, V. E. Kousky, E. S. Sarachik, and H. von Storch, 1998: On the structure and evolution of ENSO-related climate variability in the tropical Pacific. *J. Geophys. Res.*, **103**, 14 241–14 260.
- Webster, P. J., A. M. Moore, J. P. Loschnigg, and R. R. Leben, 1999: Coupled ocean–atmosphere dynamics in the Indian Ocean during 1997–98. *Nature*, **401**, 356–360.
- Woodruff, S. D., H. Diaz, J. D. Elms, and S. J. Worley, 1998: COADS Release 2 data and metadata enhancements for improvements of marine surface flux fields. *Phys. Chem. Earth*, **23**, 517–527.
- Xie, S.-P., H. Annamalai, F. A. Schott, and J. P. McCreary, 2002: Structure and mechanisms of South Indian Ocean climate variability. *J. Climate*, **15**, 864–878.
- Yu, L., and M. M. Rienecker, 1999: Mechanisms for the Indian Ocean warming during the 1997–98 El Niño. *Geophys. Res. Lett.*, **26**, 735–738.